Dynamics of Active Defects on the Anisotropic Surface of an Ellipsoidal Droplet

Martina Clairand,[1,*] Ali Mozaffari,[2,3,*] Jerôme Hardoüin,[4,5] Rui Zhang,[6] Claire Doré,[1] Jordi Ignés-Mullol,[4,†] Francesc Sagués,[4,5] Juan J. de Pablo,[2,7,‡] and Teresa Lopez-Leon[1,§]

[1]*Laboratoire Gulliver, UMR CNRS 7083, ESPCI Paris, PSL Research University, 75005 Paris, France*
[2]*Pritzker School of Molecular Engineering, The University of Chicago, Chicago, Illinois 60637, USA*
[3]*OpenEye Scientific, Cadence Molecular Sciences, Boston, Massachusetts 02114, USA*
[4]*Departament de Química Física, Universitat de Barcelona, 08028 Barcelona, Spain*
[5]*Institute of Nanoscience and Nanotechnology, Universitat de Barcelona, 08028 Barcelona, Spain*
[6]*Department of Physics, Hong Kong University of Science and Technology, Clear Water Bay, Kowloon, Hong Kong*
[7]*Center for Molecular Engineering, Argonne National Laboratory, Lemont, Illinois 60439, USA*

(Received 30 May 2023; revised 5 February 2024; accepted 17 July 2024; published 20 September 2024)

We investigate the steady state of an ellipsoidal active nematic shell using experiments and numerical simulations. We create the shells by coating microsized ellipsoidal droplets with a protein-based active cytoskeletal gel, thus obtaining ellipsoidal core-shell structures. This system provides the appropriate conditions of confinement and geometry to investigate the impact of nonuniform curvature on an orderly active nematic fluid that features the minimum number of defects required by topology. We identify new time-dependent states where topological defects periodically oscillate between translational and rotational regimes, resulting in the spontaneous emergence of chirality. Our simulations of active nematohydrodynamics demonstrate that, beyond topology and activity, the dynamics of the active material are profoundly influenced by the local curvature and viscous anisotropy of the underlying droplet, as well as by external hydrodynamic forces stemming from the self-sustained rotational motion of defects. These results illustrate how the incorporation of curvature gradients into active nematic shells orchestrates remarkable spatiotemporal patterns, offering new insights into biological processes and providing compelling prospects for designing bioinspired micromachines.

DOI: 10.1103/PhysRevX.14.031049 Subject Areas: Soft Matter

I. INTRODUCTION

Active nematics (ANs), composed of elongated self-propelling units, constitute a paradigm for active fluids, in which the interplay between activity and nematic elasticity results in the emergence of complex spatiotemporal patterns [1–4]. Beyond their intrinsic relevance in nonequilibrium physics, ANs have been identified in a range of biological systems and processes, from the reorganization of active fibers during morphogenesis to the collective dynamics of bacterial populations and tissue growth [5–8], which have often been the source of inspiration for experimental and theoretical work on *in vitro* model systems.

At equilibrium, and in the absence of external constrains, nematic liquid crystals exhibit an aligned state, in which their elongated building blocks are oriented in average along the same direction, described by the director **n**. Activity brings the system out of equilibrium, generating unbalanced stresses that induce continuous nucleation and annihilation of topological defects, singularities in the director field that autonomously move inside the material, acting as flow inducers and information carriers. While chaotic defect dynamics are typically observed in large, *in vitro*, model systems, biological functionality often requires topological defects to follow regular patterns [5–8]. However, the mechanism by which topological defects interact with their environment to produce ordered dynamics and functional outcomes remains an open question.

Frictional forces [9–13], surface viscous anisotropy [14–16], spatial patterning of active stresses [12,17–19], or confinement [20–32] have recently been used to program defect motion and induce organized flows in the material, offering new fundamental insights in the mechanisms

[*]These authors contributed equally to this work.
[†]Contact author: jignes@ub.edu
[‡]Contact author: depablo@uchicago.edu
[§]Contact author: teresa.lopez-leon@espci.fr

behind the emergence of order and associated function. Yet the effect of the substrate curvature, crucial in morphogenetic processes, has been little explored experimentally, due to the difficulties in creating controlled curved environments in which to probe model ANs.

In a pioneering work, Keber *et al.* [22] studied the effect of imposing constant curvature to a microtubule-kinesin AN, in which bundles of motor-propelled cytoskeletal filaments slide relative to each other at a fluid interface. By confining the AN to the surface of a spherical vesicle, they observed the emergence of a regular dynamic state characterized by the motion of four topologically required $+1/2$ defects [33,34], whose positions oscillated between a tetrahedral and a planar configuration. Several theoretical and numerical models have been able to reproduce these experimental results [23,24,35–37] and demonstrated the high potential of nonconstant curvature to control the dynamics of ANs [29,38,39]. Curvature gradients act as external fields inducing defect attraction toward regions of like-sign Gaussian curvature [40–44]. While these effects cannot be studied on the surface of a sphere, whose curvature is constant, Ellis *et al.* observed the curvature-induced defect segregation while investigating the behavior of a microtubule-kinesin AN on the surface of a toroidal macroscopic droplet [26]. Yet, the large size of the droplet resulted in a myriad of topological defects and the same chaotic dynamics observed in large flat surfaces. To investigate the influence of nonuniform curvature in the AN dynamics, it is crucial to consider situations of strong confinement, where the size of the confining surface is comparable to the active length scale, i.e., the average distance between defects, which is of the order of 100 μm for a microtubule-kinesin AN. In this situation, defects are usually restricted to a small number, and their trajectories and dynamics should be strongly influenced by curvature. For instance, deforming a sphere into a prolate ellipsoid could dramatically modify the regular oscillatory behavior of the four topologically required $+1/2$ defects. Curvature gradients are expected to trigger the segregation of the defects to the poles [41,42], inducing the formation of tunable rotating states never observed on the sphere [38]. Despite the interesting predictions, the influence of nonuniform curvature on the AN dynamics remains experimentally unexplored, essentially due to the difficulties of creating nonspherical closed surfaces at a microscale.

In this work, we take advantage of the physical properties of smectic liquid crystals to fabricate ellipsoidal droplets with dimensions comparable to the typical active length scale of the AN. By introducing these elongated droplets in a microtubule-kinesin active bath, we are able to stabilize an ellipsoidal AN layer at the aqueous-smectic interface of the droplet. The size of the droplets and their geometry constrain the number of defects and their dynamics, leading to the formation of well-ordered modes [45]. As in the spherical case, we observe the oscillatory motion of four topologically required $+1/2$ defects. However, curvature gradients result in new dynamical states and the spontaneous emergence of chirality, not only at the level of the defect trajectories, but also at the level of the entire droplet, which starts rotating as a solid body. In the steady state, the system oscillates between two different regimes: (i) a long-lived rotational regime, where two pairs of defects rotate around the major axis of the ellipsoid, forming counterrotating swirls at the poles, and (ii) a short-lived translational regime, triggered by bend instabilities, in which the two pairs of $+1/2$ defects commute from one pole to the other one, aligning the active flows longitudinally. Experimental results are supported by nematohydrodynamic simulations that reconstitute the dynamics observed experimentally. While the main features of the defect dynamics result from the imposed nonhomogeneous curvature, chirality spontaneously emerges from the interplay between viscous anisotropy, enforced by the smectic substrate, and hydrodynamics.

II. RESULTS AND DISCUSSION

A. Building an ellipsoidal active nematic

1. Smectic ellipsoidal droplets

Our ellipsoidal ANs consist of elongated droplets of octyl-cyanobiphenyl (8CB), a passive liquid crystal, coated by a layer of aligned microtubule bundles sheared by kinesin motors.

The fabrication of the smectic droplets relies on the temperature-induced bursting of water/8CB/water double emulsions. The latter are produced in a glass capillary microfluidic device [46], using an aqueous solution of Pluronic F-127 (P2443, Sigma) (2 wt %) as inner phase, octyl-4-cyanobiphenyl (8CB) as middle phase, and an aqueous mixture of Pluronic F-127 (2 wt%) and glycerol (60 wt %) as outer phase. More details on the protocol to produce the double emulsions are available in Sec. IV.

To obtain the ellipsoidal shape, the double emulsions must be produced and collected at a temperature ranging between 33.5° and 40.5°, so that 8CB is in the nematic phase. Upon quenching the system, a nematic-smectic phase transition is triggered, causing the destabilization and collapse of the double emulsions into ellipsoidal droplets of 8CB. This finding is noteworthy, because 8CB droplets produced by microfluidics or vortexing typically adopt a spherical shape. The molecular organization of the system in the shell geometry, prior to the formation of the droplet, seems to be the reason behind the exotic shape of the droplets generated with this method. The resulting smectic ellipsoids are metastable, and tend to become spherical after approximately 48 hours, yet their elongated shape remains stable enough to conduct experiments on the active system. For this study, we have considered ellipsoidal droplets with principal semiaxes of length $a = b = (25–45)$ μm

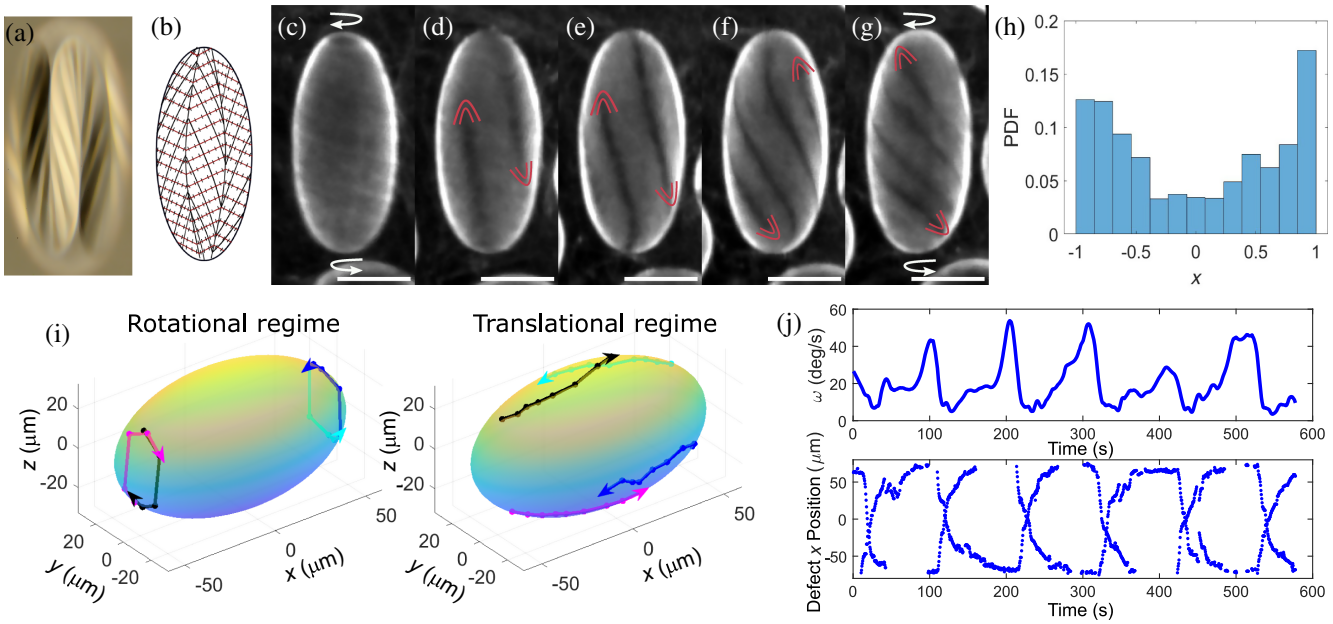

FIG. 1. Defect dynamics in the final dipolar dynamic state. (a) Crossed polarized micrograph of a smectic ellipsoidal droplet. (b) Schematic representation of the director field in (a). The smectic layers (red lines) display a chevron pattern and are perpendicular to the director field (black lines). (c)–(g) Fluorescence confocal micrographs showing half-period of the system dynamics, from $t = 0$ (c) to $t = 15$ s (g). Scale bars are 50 μm. Parabolic red lines indicate the position of $+1/2$ defects. (h) Normalized probability distribution histogram for the position of $+1/2$ defects along the major axis of the ellipsoid. (i) 3D reconstruction of the $+1/2$ defect trajectories in the rotational and translational regimes. (j) Temporal evolution of the average angular speed and defect position along the major axis of the ellipsoid. The dynamics reported in (c)–(g) was observed for 50 droplets from independent experiments. The distribution trend in (h) and the periodic oscillations in (j) were observed for all the analyzed droplets (typically 10). Abbreviation: PDF stands for probability density function.

and $c = (50\text{–}90)$ μm, choosing those with an aspect ratio of $c/a \approx 2$. This represents about one third of the droplets generated using the above protocol.

Under both bright field and polarized light, the smectic ellipsoids reveal a structure similar to that described for spherical smectic shells [47]. The most outstanding feature of their optical texture is the presence of a set of meridional lines, which connect the two poles of the ellipsoid, dividing it into crescent domains, as shown in Figs. 1(a) and 1(b). These lines represent curvature walls where **n** rotates by a constant angle. Consequently, the smectic layers, which are indicated by red lines in Fig. 1(b), are tilted in opposite directions in adjacent domains.

2. Adding an active nematic shell

To produce the ellipsoidal AN, the smectic droplets are dispersed in an aqueous active gel, where energy consuming kinesin motors cross-link and set into motion adjacent fluorescent-labeled microtubule bundles. In contrast to previous studies, where the active gel was encapsulated inside a droplet or vesicle [22,26], here the active gel constitutes the continuous phase in which the droplets are dispersed. Through the depleting action of polyethylene glycol (PEG), the bundles gradually condense at the aqueous-8CB interface to progressively form an ellipsoidal AN [48,49].

The active gel containing the passive droplets is introduced into a polyacrylamide-coated square glass capillary of 0.6 mm inner width for observation. A constant supply of adenosine triphosphate (ATP) is ensured by the addition of phosphoenolpyruvate (PEP), which regenerates the activity of the nematic film. The chemical energy in the bulk can be renewed as often as needed through the dispersing solution, right before the activity is exhausted. An extended version of the protocol is provided in Sec. IV.

The dynamic self-assembly of microtubules and motor clusters can be observed a few minutes after filling the capillary with the active mixture. The dispersing phase is populated with fluorescent filaments, tens of microns long, that continually extend and buckle, generating large active chaotic flows around the passive droplets. The progressive accumulation of active filaments on the droplet surface leads to the formation of an AN shell that becomes stiffer with time, driving the active length scale to higher values [50–52]. In the following section, we analyze the large-scale flows and remarkable defect dynamics of the ellipsoidal AN shells.

B. Dynamics of an active nematic ellipsoidal shell

1. Transient quadrupolar state

After approximately 2 hours, under the given experimental conditions, the droplet surface has accumulated

enough active material to sustain an organized state characterized by an ordered pattern of textures and flows. Although this state is a transient toward a different steady state (described below), its geometry and dynamics already capture the effect of the inhomogeneous curvature of the AN shell. In this state, each pole of the ellipsoid, where curvature is maximal, hosts a pair of $+1/2$ defects, that continuously rotate around the ellipsoid long axis, both with the same handedness, while the ellipsoid equator, where curvature is minimal, is decorated by a counter-rotating belt with zero net topological charge, containing equal number of alternating $+1/2$ and $-1/2$ defects; see Fig. 5, Movie 1 in Supplemental Material [53], and Appendix A for a detailed analysis of this state.

This circulating defect configuration alternates with episodes where the equatorial belt vanishes and the $+1/2$ defects cease to rotate and switch poles. After this transit, the original rotating regime is quickly recovered, preserving the original chirality of the defect motion. The persistence of the rotating regime is further evidenced by the fact that defect residency time is maximal at the poles, where the two pairs of $+1/2$ defects rotate, and at the equator, where the defect band with zero net topological charge forms; see Fig. 5.

2. Dipolar state: The final dynamic state

As time progresses, the amount of active material adsorbed on the ellipsoid surface increases. Since activity is kept constant over time by periodically renewing the active bath through the open end of the glass capillary (see Sec. IV), the AN shell is likely to become stiffer during this progressive increase of its density. This will cause a progressive increase of the active length scale, $l_\alpha \propto \sqrt{K/\alpha}$, where α is the activity and K the nematic elastic constant [3]. Consequently, textures and flows at larger length scales and lower defect densities are stabilized. This results in the suppression of the equatorial band of defects, leading to dynamics regulated by the motion of only two pairs of $+1/2$ defects.

Similarly to what occurs in the transient state, the dynamics switches periodically between a rotational regime, where the two pairs of $+1/2$ defects form swirls at the ellipsoid poles, and a translational regime, where the defects commute from pole to pole. A half-period of this oscillatory dynamics is shown in Figs. 1(c)–1(g), and representative defect trajectories for the rotational and translational regimes are plotted in Fig. 1(i). Only one defect from each pair is visible at any given time.

The *rotational regime*, is now characterized by the *counterrotation* of the two pairs of $+1/2$ defects around the poles, as depicted in Figs. 1(c) and 1(i) (left) and Movie 2 in Supplemental Material [53]. The new arrangement conforms to a dipolar structure, with loss of equatorial mirror symmetry, where the flows are well aligned along latitudinal lines, as shown in Fig. 1(c). This pattern is compatible with the smectic structure of the substrate, with smectic layers [red segments in Fig. 1(b)] setting the easy flow direction [14,16].

Transversal bend instabilities act to relax the accumulated stress on this aligned configuration, setting the onset of the *translational regime*, where longitudinal flows trigger the migration of defects toward opposite poles, as shown in Figs. 1(d)–1(g), and 1(i) (right). Defect migration results in the formation of four crimps in the form of dark longitudinal bands, two of which are visible at any given time. Once defects have migrated toward the opposite pole, bands spontaneously tilt and eventually the first half of this dynamical cycle is completed by the formation of one swirl at each pole. In the second half of the cycle, the entire process is repeated, and the defect pairs return to their initial positions. Interestingly, the chirality of the flows, randomly selected upon AN formation, is preserved throughout the process. To visualize the defect trajectory over several dynamical cycles, see Movie 3 and the left-hand panel of Movie 4 in Supplemental Material [53].

To clearly visualize the effect of curvature on the defect location, we measured the probability of defect residence along the major axis of the ellipsoid, as shown in the histogram of Fig. 1(g). Indeed, results indicate that $+1/2$ defects preferentially accumulate at the poles, where curvature is maximal, in agreement with theoretical predictions [29,38,39]. Both intrinsic and extrinsic couplings between the curvature tensor and the director field could, in principle, be responsible for this behavior. Mean (extrinsic) curvature and Gaussian (intrinsic) curvature, defined respectively as the sum and product of the two principal curvatures of the surface at a point, $\kappa_M = \kappa_1 + \kappa_2$ and $\kappa_G = \kappa_1\kappa_2$, are minimal at the equator of the ellipsoid and maximal at the poles. In the typical ellipsoids considered in this work, κ_G is in the range $[1.6 \times 10^{-4}, 1.6 \times 10^{-3}]$ μm^{-2}, while κ_M varies in the range $[3.4 \times 10^{-2}, 8.0 \times 10^{-2}]$ μm^{-1}. According to previous studies, mean curvature is expected to act as an external field aligning the director along the direction of minimal principal curvature, that is, along the main axis of the ellipsoid, reducing bend elastic energy. In our experiments, we observe the opposite tendency, the microtubule bundles bend in the direction of maximal principal curvature [54–56]. As we discuss in the next section, this is due to the friction anisotropy imposed by the ellipsoidal subtract, which favors flow alignment along latitudinal lines. On the other hand, in order to reduce elastic energy costs, Gaussian curvature is expected to attract positive defects toward regions of maximal positive Gaussian curvature, that is, the poles of the ellipsoid, as observed in the experiments [54,55,57]. Therefore, Gaussian curvature seems to be the main force driving the defects toward the poles, although we cannot neglect other potential effects of the curvature tensor, which can intervene not only in the elastic term of the free energy, but also in the surface anchoring term, or in terms involving flow.

Regarding the defect dynamics, Fig. 1(j) shows the average angular speed of defects as a function of their position along the major axis of the ellipsoid. A pattern of in-phase oscillations is clearly evidenced, where the local maxima of the angular velocity correspond to the rotational regime and local minima to the translational regime in which defects commute between poles. Additional details on the periodic oscillation of topological defects are presented in Appendix B, including the angular distances between defects as shown in Fig. 6 and Movie 4 in Supplemental Material [53].

In summary, our findings demonstrate the formation of a steady-state oscillatory dynamics when an AN is confined to the surface of a smectic ellipsoidal droplet. Both gradients of curvature and viscous anisotropy couple to control the active flows, leading to remarkably organized dynamic patterns, driven by the chiral motion of four $+1/2$ defects. This behavior is essentially different from the tetrahedral-to-planar switching state observed in spherical geometries. The persistent antiparallel rotation of the defect pairs also has an impact on the overall hydrodynamics, leading to a solid body rotation of the ellipsoids that will be essential to understand the dynamics of the AN shell, as we argue below. In the following section, we disentangle the role of curvature and viscous anisotropy by resorting to numerical simulations.

C. Coupling between curvature gradients, friction anisotropy, and hydrodynamic flows

1. Curvature effects

The final dipolar state observed experimentally is simulated by a thin shell of AN in a tangent plane between two concentric ellipsoids. Initially, we neglect the effects of the underlying smectic layers and focus on the impact of curvature gradients on the trajectories and dynamics of defects.

In the absence of active stresses, each pole is occupied by a pair of $+1/2$ defects, with the director field tangentially aligned along the major axis of the ellipsoid to minimize elastic free energy. This configuration allows for a nearly uniform alignment of the director field in regions with low curvature. The active stresses bring the system out of this equilibrium configuration, and the defects start to rotate indefinitely on the antipodal points of a circumference centered at each pole of the ellipsoid; see Movie 5 in Supplemental Material [53] for a visual representation of this process. Away from the poles, the director field adopts a steady configuration with a slight tilt relative to the major axis. As the activity strength increases, the defects rotate faster, and the director field tilts further from the major axis. Similar to our experimental observations, when the activity surpasses a critical value, the defects display spiral trajectories and migrate toward opposite poles. The system develops well-organized spatiotemporal patterns, with defect dynamics that periodically switch from a circulation-dominant motion at the regions of maximal curvature to linear translation near the equatorial plane; see Movie 6 in Supplemental Material [53]. Note that defects maintain their sense of rotation as they travel toward the opposite side of the ellipsoid, resulting in an inversion of the handedness at the poles every half-period, as shown in the sequence of images in Figs. 2(a)–2(f). We further explore the residence time of the defects through a probability distribution function for finding defects along the major axis of the active system. Figure 2(g) reveals that defects are primarily found in the regions of maximum curvature. At the higher values of activity, the residence time at the poles decreases and the histogram shown in Fig. 2 becomes more uniform.

The dynamics described in these simulations, which we refer to as *frictionless system simulations*, reproduce the periodic commutation between the rotational and translational regimes. However, in contrast with experiments, there is an inversion of the handedness at the poles every half-period. Therefore, the experimental final state shown in Fig. 1 cannot be explained solely on the grounds of

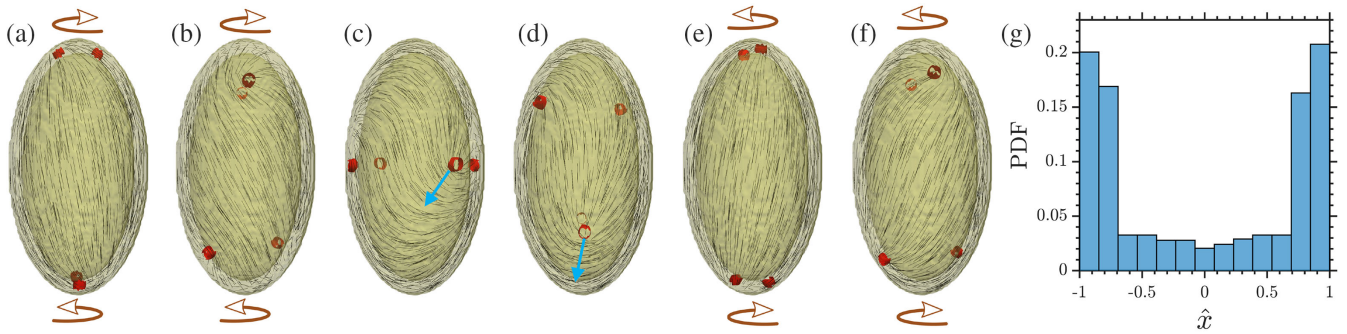

FIG. 2. (a)–(f) Simulation results for the spatiotemporal evolution of the nematic texture of an AN shell confined between two concentric ellipsoids, shown in a series of snapshots. The sense of rotation of defects at the poles is denoted by brown arrows. The red isosurfaces indicate the location of the four $+1/2$ defects and the black lines are the local director field. The blue arrow shows the direction of self-propulsion of the $+1/2$ defect. (g) Probability distribution histogram for the location of the defects along the ellipsoid major axis. The defect position is normalized with the average of the inner and outer shell major axes.

geometric considerations, and other parameters involved in the steering of the defects' pathways must be examined. Indeed, the smectic droplet under the AN shell displays a textured surface. As discussed in Appendix C, we believe that the complex dynamics of the active system and the trajectories of the self-propelled $+1/2$ defects are influenced by the anisotropic friction enforced by the smectic substrate. To address this question, in the next section, we consider the effect of anisotropic friction in our simulations.

2. Role of friction anisotropy

The effect of the smectic layers in contact with the AN is accounted for by adding a frictional damping force to the equations of motion that penalizes the fluid flow along certain directions, with a strength defined through a diagonal tensor **f** [Sec. IV, Eq. (5)]. More details about this approach can be found in Appendix C, where we discuss the role of frictional damping in the regulation of planar active flows. We first consider a uniform frictional pattern that penalizes flow along the long axis of the shell, aiming to mimic the structure of smectic layers, which provide an easy flow direction roughly parallel to the equatorial plane; see red lines in Fig. 1(b). In agreement with experiments, we observe topological defects organized in pairs at the poles, counterrotating about the major axis of the ellipsoid. As defects spin around each other, the director field gets slightly tilted away from its original orientation. This simulation shows that the incorporation of anisotropic frictional damping forces improves agreement with the residence time distribution of the defects along the long axis observed in experiments, but fails to accurately predict the defects' trajectories and, even more importantly, the handedness of rotation of the defects at the poles, see Movie 7 in Supplemental Material [53].

3. Effect of external flow fields

The discrepancies between the experimental and simulation results prompted us to adopt a nonuniform frictional pattern that embodies the complex interplay between the hydrodynamic interactions of the ellipsoidal droplets with the nearby capillary wall and the smectic structure of the inner ellipsoidal droplets. The proposed frictional pattern imposes two favorable paths that are almost mutually perpendicular. Near the poles, preferential lanes orient parallel to the equator, while on the main body, the easy direction is tilted 25° with respect to the ellipsoid major axis; see Fig. 3(a). To rationalize this complex pattern, we need to investigate the rigid body behavior of the experimental droplets when they are dispersed in the active bath.

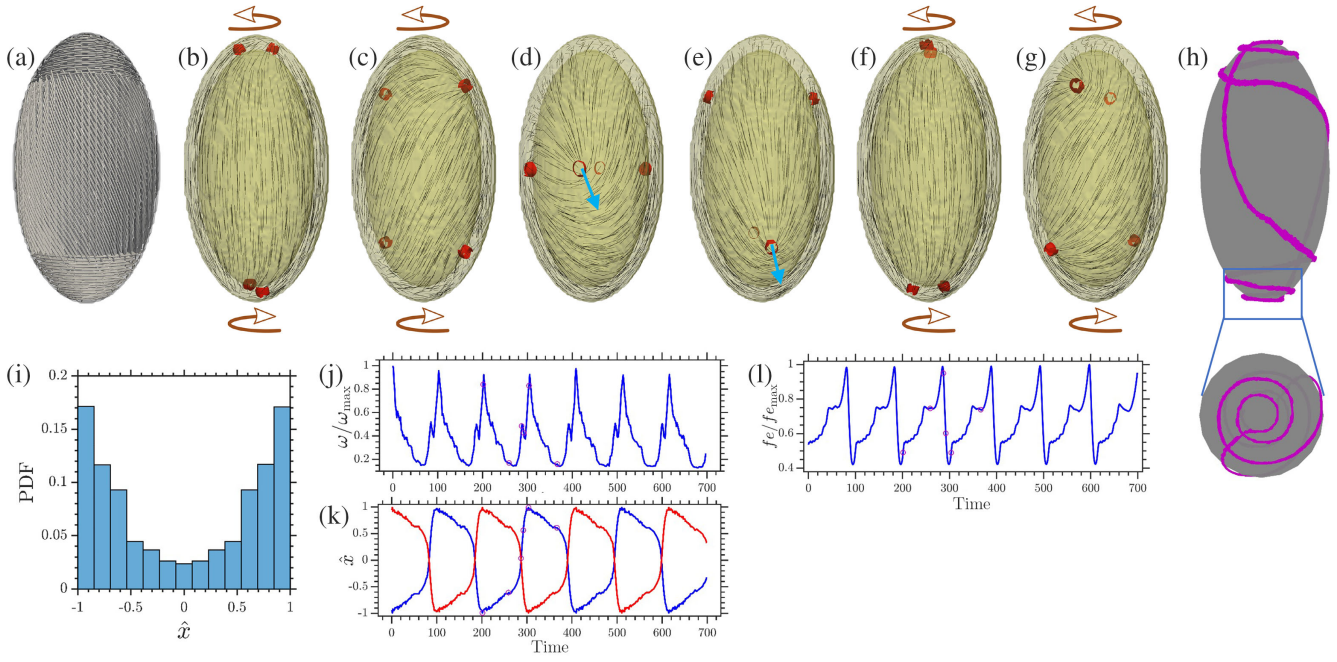

FIG. 3. (a) Easy flow pattern resulting from the anisotropic frictional damping used in this simulation. (b)–(g) Evolution of the nematic director (black lines) and the position of defects (red isosurfaces), with arrows indicating the direction of circulation at the poles. The direction of motion of $+1/2$ defect is indicated by a blue arrow. (h) Side and top view of a single defect trajectory, which shows the spiraling motion at the poles and a linear translation away from the poles. (i) Probability distribution histogram for the position of defects along the long axis of the ellipsoid. (j) Time evolution of the magnitude of average angular velocities of defects. (k) Normalized position of two defects propelling from opposite poles of the ellipsoid as a function of simulation time. (l) Variation of the elastic free energy of the system. The six purple open circles marked on the plots in (j)–(l) correspond to the snapshots of (b)–(g), respectively. Positions are normalized with the average of the major axes of the inner and outer shells.

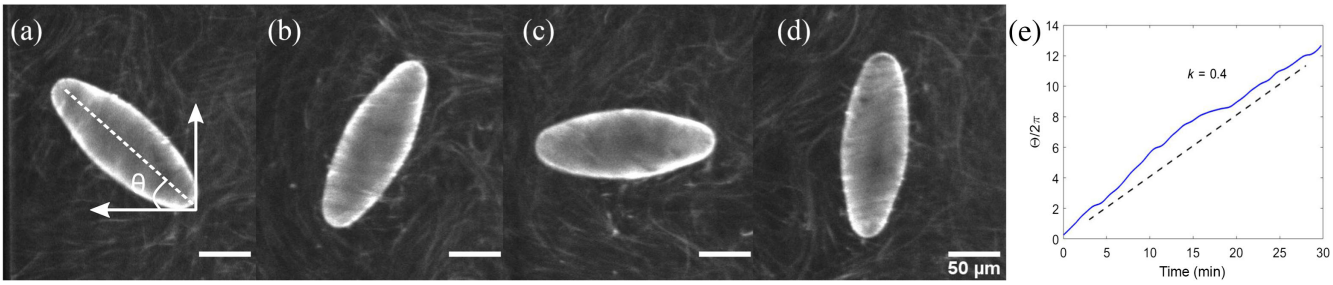

FIG. 4. (a)–(d) Fluorescence confocal micrographs of an ellipsoid in the bipolar state showing a solid body rotation; images were taken every 60 s. (e) Temporal evolution of the normalized orientation of the major axis of the ellipsoid, showing a constant angular speed. The dashed line is a slope of 0.4 rotations per minute.

Figure 4 shows the temporal evolution of the orientation of the major axis θ of the droplet with respect to the horizontal axis. Although the confining volume inside the capillary is large compared to the droplet size, our analysis is restricted to two dimensions, since buoyancy keeps the droplet close to the top wall. One can appreciate that the rotation angle $\theta(t)$ increases almost linearly with time for the final dipolar regime. These results suggest that the periodic final dynamics on the active shell is connected to the persistent rotations of the droplet, which arise from hydrodynamic interactions of the droplet with the confining boundary.

In order to shed light on these findings, we consider two defect pairs counterrotating at the poles, while we adjust the boundary conditions close to the surface of the ellipsoid, to reproduce the experimental configuration (Movie 8 in Supplemental Material [53]). The spinning behavior of the defects induces strong shear flows in the thin gap between the droplet and the nearby substrate with opposite signs at the poles. This results in a net hydrodynamic torque that promotes a rigid body rotation of the ellipsoid perpendicularly to its major axis. Interestingly, as the ellipsoid continuously rotates, the surrounding hydrodynamic force couples to the anisotropic friction of the droplet, at the AN-smectic interface, leading to a resultant easy flow pattern that determines the navigation of defects. This hydrodynamic force is stronger at the equatorial region than at the poles, which are farther from the capillary wall, explaining the need to impose a nonuniform effective frictional pattern, deviating from the smectic texture only at the central part or the ellipsoid.

The hybrid template shown in Fig. 3(a) successfully replicates the dynamics observed for the final dynamic state in our experiments. Two pairs of $+1/2$ defects periodically oscillate between two regimes, giving rise to counterrotating vortices at the two opposite ends of the ellipsoid and to a linear translation away from the poles, as shown in Figs. 3(b)–3(g). Note that this last configuration originates from the extensile nature of the active stresses, which induce diagonally oriented bending instabilities. Furthermore, the duration of the rotational regime being larger than that of the linear translation leads to a higher likelihood for spotting defects at the poles, see Fig. 3(i), thereby explaining the propensity of defects for attraction to regions with higher positive curvature displayed in Fig. 3(h). The pulse of the defect motion is further regulated by the anisotropic friction of the hybrid pattern which, in close agreement with experimental observations, see Fig. 1(g), amplifies the angular speed during circulatory motion at the poles and minimizes it near the equator of the droplet, as evidenced in Figs. 3(j) and 3(k). Note that the open circles in Figs. 3(j)–3(l) correspond to time series snapshots displayed in Figs. 3(b)–3(g). The continual oscillatory behavior between the two regimes can be understood by analyzing the temporal evolution of elastic free energy. At the poles, where defects reach the highest angular velocity, the elastic free energy is minimized. By injecting energy into the system, uniformly aligned active units are subject to bending instabilities, thereby enabling defects to escape from the poles and to travel diagonally toward the midplane, where the elastic free energy is maximized, as shown in Fig. 3(l). Notably, the chirality of the defect rotation persists over many periods, despite their continual exchange, in agreement with experiments. The final defect trajectories on AN ellipsoids are shown in Movie 9 and are translated into the spatiotemporal variations of the nematic texture displayed in Movie 10 in Supplemental Material [53].

III. FINAL REMARKS AND CONCLUSIONS

We have presented an experimental system and corresponding numerical simulations to explore the rich dynamics of an active nematic fluid when confined to an ellipsoidal surface. The new perspectives brought by this study refer both to the experimentally designed platform itself and to the revealed dynamical aspects. We use microfluidics and the elastic properties of smectic liquid crystals to produce ellipsoidal droplets with dimensions similar to the intrinsic length scale of the AN (approximately 100 μm). These droplets provide the appropriate conditions to investigate the coupling between confinement, nonuniform curvature, viscous anisotropy, and hydrodynamics. The observations are interpreted by means of a full scheme of nematohydrodynamic equations.

Our study reveals the strong influence of curvature gradients in the orderly dynamics of an ellipsoidal AN. As in the spherical case, we observe four topologically required $+1/2$ defects that display oscillatory dynamics. However, the presence of curvature gradients dramatically impacts the choreography of the four defects and, as a result, the dynamics of the whole ellipsoid. A first observation is the pronounced attraction exerted by the regions of maximal curvature, the poles of the ellipsoid, on the positive defects. Gaussian curvature seems to be the main driving force playing the role of a global field attracting positive defects toward the poles [57], although this effect might also be influenced by other potential couplings between the director and the curvature tensor, which can be present not only in the elastic term, but also in the surface anchoring term, or in terms involving flow.

Defect attraction toward the poles results in the spontaneous emergence of chirality. In the steady state, two pairs of $+1/2$ defects rotate at the poles of the ellipsoid generating two counterrotating swirls. Remarkably, the chirality of the resulting twisting motion is randomly selected upon AN formation, and is subsequently preserved. This is true even when the large-scale alignment imposed by the rotating poles succumbs to the well-known bend instability of an aligned extensile AN, leading to the periodic relocation of defects toward the opposite pole. Interestingly, this mirror symmetry breaking is bottom-up transmitted to the ellipsoid when placed near the wall of the containing cell, making it rotate as a solid body.

Numerical simulations show that this intriguing steady state results from a delicate interplay between (i) the intrinsic activity of the nematic fluid, (ii) the inhomogeneous curvature and viscous anisotropy of the surface where it resides, and (iii) the hydrodynamic interactions with the surrounding fluid. Here we employ a model based on dynamical schemes that reproduce the full nematodynamic equations describing all involved fluids. As demonstrated above, the complexity of the reported dynamics could not be captured otherwise. This is a clear advance with respect to earlier studies of AN shells [22,26], where simulations used a simplified approach considering defects as pointlike particles that interact via elastic forces and torques.

These results may contribute to a deeper understanding of fundamental dynamical aspects of active nematic fluids when performing under nonuniformly curved confining landscapes. Although our study focuses on the ellipsoidal geometry, the experimental platform here described opens new avenues for the generation of nonspherical microdroplets with other geometries. The final shape of the droplet is expected to depend on the liquid crystal organization within the precursor shells, which can be controlled through different parameters, including shell thickness, molecular anchoring of the liquid crystal molecules at the interfaces, elastic properties of the liquid crystal, etc.

Finally, we remark that both the emergence of chirality and the role of topological defects in self-organizing processes are fundamental issues in biology. In particular, defects in the orientational field describing intracellular or supracellular organization have been recently identified as topological morphogens controlling the shape of both eukaryotes and prokaryotes [58]. These processes encode functions as important as bacterial colony survival [6,7,59], apoptotic cell extrusion in epithelia [60], and animal morphology [5,61]. Hydra, a small freshwater animal with remarkable regeneration properties, provides a beautiful example of the relevance of defects in those morphogenetic processes [5]. During animal regeneration from a tissue fragment, positive topological defects in a actin or myosin cytoskeletal active nematic lead to regions of positive Gaussian curvature (mouth, tip of tentacles) while negative defects give rise to regions of negative Gaussian curvature (base of tentacles), showing the existence of a strong coupling between topological defects and substrate curvature. Our study offers a simplified model system that can effectively address these issues, potentially fostering novel ideas and perspectives in the study of living systems and in the design bioinspired autonomous micromachines.

IV. MATERIALS AND METHODS

A. Experiments

1. Production of smectic droplets

(a) *Microfluidic device fabrication.*—Ellipsoidal droplets were produced from thin double emulsions [W (water)/LC (liquid crystal)/W] prepared using glass capillary microfluidics [46]; see sketch in Fig. 8. Our device is made of two cylindrical capillaries of 1 mm outer diameter inserted into the opposite ends of a 1.02 mm square capillary. The two cylindrical capillaries are tapered on one side using a micropipette puller. Their tips are cut with a microforge to reach inner diameters of 60 μm, for the injection capillary, and 120 μm, for the collection capillary. The injection capillary, employed to inject the inner phase, is immersed in a solution containing 0.2 vol % *n*-octadecyl-trimethoxysilane (376213, Sigma), 20 vol % chloroform, and 79.8 vol % hexane, for 5 min to render its surface hydrophobic. Subsequently, the capillary is washed for 2 min with chloroform, dried with compressed air, and heated for at least 8 h at 200 °C. The cylindrical capillaries are then inserted facing each other into the square capillary. Their tips are aligned on the microscope, maintaining a separation distance of approximately 60 μm. Dispensing needles are finally fixed at the three inlets of the device to inject the three phases constituting the double emulsions.

(b) *Production of smectic shells and ellipsoidal droplets.*—We introduce a 2 wt % Pluronic 127 solution

through the injection capillary, and 8CB liquid crystal through the square capillary, which coflow forming a composed jet at the entrance of the collection cylindrical capillary. The outer solution, composed of Pluronic 127 2 wt % and glycerol 60 wt % in Milli-Q water, is pumped from the other side of the square capillary, flow focusing the composed jet into the collection capillary. Such composed jet becomes unstable and breaks up into double emulsions. The device is locally heated at a temperature ranging between 33.5 °C and 40.5 °C, to maintain the 8CB LC in the nematic phase. We observe a stable dripping regime at typical flow rates of 100, 400, and 7500 μLh^{-1} for the inner, middle, and outer fluids, respectively. The shells are then collected in a solution with the same composition as the inner phase, preheated at 60 °C. In a second step, the collection vial is kept at room temperature for 15 min to trigger the N (nematic)/SmA (smectic-A) transition of the LC, inducing the bursting of the shells and the formation of the ellipsoidal droplets. Under these conditions, 60% of the resulting smectic droplets have an elongated shape, and among them, one to two thirds fit the standards of what we consider in our experiments as model ellipsoids. These are prolate spheroids with principal semiaxes lengths $a = b = 30 \pm 10$ μm and $c = 70 \pm 20$ μm, yielding an aspect ratio $c/a \approx 2$. Therefore, about 30% of the smectic shells are transformed into model ellipsoids. Smectic droplets are collected and placed into the vial containing the active material. A few microliters of this solution are introduced into a square capillary for observation.

2. Microtubule polymerization

Polymerization was carried out by incubating at 37 °C for 30 min an aqueous mixture of heterodimeric (α,β)-tubulin from bovine brain (Brandeis University Biological Materials Facility), M2B buffer (80 mM Pipes, 1 mM EGTA, and 2 mM $MgCl_2$) (Sigma, P1851, E3889, and M4880, respectively), dithiothrethiol (43815, Sigma) reducing agent, and a nonhydrolysable guanosine triphosphate (GTP) analog GMPCPP [guanosine-5′-[(α,β)-methyleno] triphosphate] (NU-405, Jena Biosciences) that suppresses the dynamic instability of Microtubules (MTs). By adjusting GMPCPP concentration, tubulin heterodimers associate in a controlled way to produce a high-density suspension of short MTs (1–2 μm). For fluorescence observation, 3% of the tubulin was labeled with Alexa 647 (A20006, Thermo Fisher Scientific). The final solution was kept at room temperature for 5 h, frozen in liquid nitrogen, and stored at −80 °C for future use.

3. Kinesin expression

In this experiment, heavy-chain kinesin-1 K401-BCCP-6His from *Drosophila melanogaster* [truncated at residue 401, fused to biotin carboxyl carrier protein (BCCP), and labeled with six histidine tags] was expressed in *Escherichia coli* using the plasmid WC2 from the Gelles Laboratory (Brandeis University) and purified with a nickel column. After dialysis against 500 mM imidazole buffer, the concentration of the suspension was adjusted to 60% (wt/vol) with a sucrose solution and estimated by means of absorption spectroscopy. The final protein solution was stored at −80 °C until used.

4. Active solution preparation

Kinesin motor clusters were prepared by incubating biotinylated kinesins with tetrameric streptavidin (43-4301, Invitrogen) at a 2:1 stochiometric ratio, for 30 min, under the reducing action of 2 μM DTT (dithiothreitol). The resulting suspension was mixed with a standard solution containing the M2B buffer and a PEG (20 kDa; 95172, Sigma) depleting agent. To prevent protein denaturation and photobleaching during the fluorescence acquisition, 5.8 mM DTT, 0.2 $mg\,mL^{-1}$ glucose oxidase, 0.04 $mg\,mL^{-1}$ catalase, 2.1 mM Trolox, and 3.5 $mg\,mL^{-1}$ glucose antioxidants were incorporated to the mixture. The activity of the system was provided by chemical energy in the form of ATP (A2383, Sigma) (1.5 mM) and was constantly regenerated by the action of phosphoenolpyruvate (PEP) (P7127, Sigma) and pyruvate kinase/lactate dehydrogenase (PK/LDH) (434301, Invitrogen).

5. Sample preparation

The active gel was prepared by introducing 1 μL of microtubule suspension in 5 μL of active solution. Biocompatility and microtubule adsorption at the water-oil interface, in subsequent steps, were facilitated by the addition of 1 μL of Pluronic F-127 (P2443, Sigma) 17 wt % and 1 μL of Tween-80 (P1754, Sigma) 17 wt % surfactants to the previous solution. Afterward, 1 μL of the smectic droplets suspension was carefully incorporated. The final solution was gently introduced into a 0.6 mm square capillary, previously treated with an acrylamide brush. The latter coating was prepared by following reported protocols [62] to prevent the adhesion of the active material to the glass walls. The use of a square capillary of such dimensions has several advantages over a standard flow cell [27]. First, it allows us to manipulate small amounts of the active gel and to concentrate the droplets in a small volume. Second, the chemical energy (ATP) of the active bath can be renewed as often as needed since one of the capillary ends is kept open. Lastly, in the capillary, the evaporation of the active solution is reduced with respect to a standard flow cell.

6. Imaging

Active nematics observation, based on the fluorescence of labeled microtubules, was performed using a spinning

disk confocal on a Nikon TI-E inverted microscope equipped with a Perfect Focus System for continuous maintenance of focus. Images were typically captured every 500 ms with a 10× objective and an Andor Zyla 4.2MP camera operated with NiS-Elements software. With the ×10 objective, the confocal mode is not perfectly reached, giving rise to a depth of field of tens of microns, which allows us to focus the whole droplet hemisphere, a few microns in depth. Images for the 3D reconstruction of defect trajectories [see Figs. 5(g) and 1(f) and Movie 3 in Supplemental Material [53]] were acquired by simultaneously capturing four different planes, two of the top and two of the bottom planes of the droplet, at a rate of 0.7 frames/s.

7. Image analysis

Defect tracking was performed from confocal z-projection images, using the MANUAL TRACKING Fiji/imageJ plugin. For each frame of a movie, defects were identified as dark spots with cometlike shape. 2D trajectories were further computed with a homemade MATLAB program. The angular speed of defects was calculated from their 3D trajectories, reconstructed by projecting 2D trajectories onto the ellipsoidal surface.

B. Simulations

1. Governing equations

The systems considered here are described in terms of a nematic tensorial order parameter $\mathbf{Q}$ and a flow field $\mathbf{u}$. The standard theory of active nematodynamics is used to quantify their spatiotemporal evolution. For uniaxial systems, the nematic order parameter is written in the form $\mathbf{Q} = S(\mathbf{nn} - \mathbf{I}/3)$ where unit vector $\mathbf{n}$ is the nematic director field and S is an order parameter that measures the extent of orientational ordering. The evolution of this nonconserved order parameter obeys the strongly nonlinear equation,

$$\left(\frac{\partial}{\partial t} + \mathbf{u}\cdot\boldsymbol{\nabla}\right)\mathbf{Q} - \mathbf{S} = \Gamma\mathbf{H}, \tag{1}$$

where the advection term is generalized by $\mathbf{S} = (\xi\mathbf{A} + \boldsymbol{\Omega})\cdot[\mathbf{Q} + (\mathbf{I}/3)] + [\mathbf{Q} + (\mathbf{I}/3)]\cdot(\xi\mathbf{A} - \boldsymbol{\Omega}) - 2\xi[\mathbf{Q} + (\mathbf{I}/3)](\mathbf{Q}:\nabla\mathbf{u})$, which accounts for the response of the nematic order parameter to the symmetric $\mathbf{A}$ and antisymmetric $\boldsymbol{\Omega}$ parts of the velocity gradient tensor ($\nabla\mathbf{u}$). Here, ξ is the flow aligning parameter, chosen to be $\xi = 0.7$ for flow aligning elongated units. The molecular field $\mathbf{H} = -[(\delta\mathcal{F}_{\mathrm{LdG}}/\delta\mathbf{Q}) - (\mathbf{I}/3)\mathrm{Tr}(\delta\mathcal{F}_{\mathrm{LdG}}/\delta\mathbf{Q})]$ embodies the relaxational dynamics of the nematic, which drives the system toward the configuration with minimum Landau–de Gennes free energy:

$$\mathcal{F}_{\mathrm{LdG}} = \int_V f_{\mathrm{LdG}}\mathrm{d}V. \tag{2}$$

The free-energy density f_{LdG} is the sum of bulk and elastic energies given by

$$f_{\mathrm{LdG}} = \frac{A_0}{2}\left(1 - \frac{U}{3}\right)\mathrm{Tr}(\mathbf{Q}^2) - \frac{A_0 U}{3}\mathrm{Tr}(\mathbf{Q}^3) + \frac{A_0 U}{4}[\mathrm{Tr}(\mathbf{Q}^2)]^2 + \frac{L}{2}(\nabla\mathbf{Q})^2. \tag{3}$$

The relaxation rate is controlled by the collective rotational diffusion constant Γ. The phenomenological coefficient A_0 sets the energy scale, U controls the magnitude of the order parameter, and L is the elastic constant in the one-elastic constant approximation. At the boundary surface with unit normal $\boldsymbol{\nu}$, the anchoring condition is imposed by adding a surface term to the free energy, $\mathcal{F}_{\mathrm{surf}} = \int_{\partial V} f_{\mathrm{surf}}\mathrm{d}S$. The fourth-order Fournier-Galatola free-energy density is adopted to apply the degenerate planar anchoring boundary condition,

$$f_{\mathrm{surf}} = \frac{1}{2}\mathcal{W}(\bar{\mathbf{Q}} - \bar{\mathbf{Q}}_\perp)^2 + \frac{1}{4}\mathcal{W}(\bar{\mathbf{Q}}:\bar{\mathbf{Q}} - S^2)^2, \tag{4}$$

where $\mathcal{W}$ controls the anchoring strength, $\bar{\mathbf{Q}} = \mathbf{Q} + \frac{1}{3}S_{\mathrm{eq}}\boldsymbol{\delta}$, its projection to the surface $\bar{\mathbf{Q}}_\perp = \mathbf{p}\cdot\bar{\mathbf{Q}}\cdot\mathbf{p}$, and $\mathbf{p} = \mathrm{I} - \boldsymbol{\nu}\boldsymbol{\nu}$.

The local fluid density ρ and velocity $\mathbf{u}$ are governed by the generalized incompressible Navier-Stokes equations, modified by a frictional dissipative term:

$$\rho\left(\frac{\partial}{\partial t} + \mathbf{u}\cdot\nabla\right)\mathbf{u} = \boldsymbol{\nabla}\cdot\boldsymbol{\Pi} - \mathbf{f}\cdot\mathbf{u}. \tag{5}$$

The total asymmetric stress tensor $\boldsymbol{\Pi} = \boldsymbol{\Pi}^{\mathrm{p}} + \boldsymbol{\Pi}^{\mathrm{a}}$ is a sum of a passive and an active stress, and $\mathbf{f}$ is the diagonal tensor describing frictional damping between the nematic fluid and the underlying substrate. The viscoelastic properties of the nematic are lumped in the passive stress, which is the sum of the viscous and elastic terms,

$$\boldsymbol{\Pi}^{\mathrm{p}} = 2\eta\mathbf{A} - P_0\mathbf{I} + 2\xi\left(\mathbf{Q} + \frac{\mathbf{I}}{3}\right)(\mathbf{Q}:\mathbf{H}) - \xi\mathbf{H}\cdot\left(\mathbf{Q} + \frac{\mathbf{I}}{3}\right) - \xi\left(\mathbf{Q} + \frac{\mathbf{I}}{3}\right)\cdot\mathbf{H} - \boldsymbol{\nabla}\mathbf{Q}:\frac{\delta\mathcal{F}_{\mathrm{LdG}}}{\delta\boldsymbol{\nabla}\mathbf{Q}} + \mathbf{Q}\cdot\mathbf{H} - \mathbf{H}\cdot\mathbf{Q}, \tag{6}$$

where $\mathbf{A}$ is the strain rate tensor and the active stress,

$$\boldsymbol{\Pi}^{\mathrm{a}} = -\zeta\mathbf{Q}. \tag{7}$$

Here, η is the isotropic viscosity, P_0 is the isotropic bulk pressure, and ζ measures the activity strength. A flow is generated when $\mathbf{Q}$ has a spatial gradient with $\zeta > 0$ for extensile systems and $\zeta < 0$ for contractile systems.

2. Numerical method

We employ a hybrid lattice Boltzmann method to solve the coupled governing partial differential equations [Eqs. (1) and (5)] [21,28,63,64]. The time integration is performed using an Euler forward scheme; the spatial derivatives are carried out using a second-order central difference and the coupling is enforced by exchanging local fields between these algorithms at each time step. Simulations were performed on a three-dimensional lattice where the active layer was confined between two ellipsoids with a uniform shell of thickness 4 lattice spacing, and the inner prolate spheroid's semiminor and semimajor axes were chosen to be 20, 20, 40, respectively, giving the aspect ratio of the inner shell to be slightly smaller than 2 (uniform thickness of the shell results in a different aspect ratio for the outer shell, slightly smaller than 2). All dimensions are expressed in lattice units. The medium viscosity was set to $\eta = 1/6$, and the collective rotational viscosity to $\Gamma = 0.3$. We chose the following parameters throughout the simulation: $A_0 = 0.1$, $L = 0.1$, $U = 3.0$ (giving $S = 0.5$). Planar anchoring conditions with strength $\mathcal{W} = 0.1$ and a no-slip velocity field at the surface of the inner and outer ellipsoids were enforced. The system was initialized with the director field tangentially oriented along the major axis. The thin shell confined between the ellipsoids was activated by applying uniform extensile active stresses to the nematic.

ACKNOWLEDGMENTS

This project has received funding from the European Union's Horizon 2020 research and innovation program, under the Marie Sklodowska-Curie Grant Agreement No. 754387, and from the French National Research Agency, under Grant No. ANR-18-CE09-0028-02. It was also supported by a STSM Grant from COST Action CA17139. The theoretical work was funded by the National Science Foundation, through the University of Chicago MRSEC under Grant No. DMR-2011854. J. I.-M., and F. S. acknowledge funding from MICIU/AEI/10.13039/501100011033 (Grants No. PID2019–108842 GB-C22 and No. PID2022-137713NB-C21). We thank B. Martínez-Prat, M. Pons, A. LeRoux, and G. Iruela (Universitat de Barcelona) for their assistance in the expression of motor proteins. We thank Brandeis University MRSEC Biosynthesis facility (supported by NSF MRSEC 2011846) for providing the tubulin.

APPENDIX A: DEFECT DYNAMICS IN THE TRANSIENT QUADRUPOLAR STATE

The dynamics of this state exhibits clear switching behavior, as indicated by the motion of defects. Specifically, the system commutes regularly between a long-lived regime of rotationally moving defects that is interspersed with episodes where defects feature translational motion. A half-period of this dynamics is reproduced in Figs. 5(a)–5(d). Figure 5(g) shows the trajectories described by the defects during a certain representative time for both the rotational and the translational regimes.

Figures 5(a) and 5(d) show two snapshots of the droplet in the *rotational regime*. In this regime, each pole of the ellipsoid hosts a pair of $+1/2$ defects, while the ellipsoid equator is decorated by a belt of $+1/2$ and $-1/2$ defects. Positive (self-propelled) and negative (dragged) defects are highlighted in red and cyan, respectively, in Figs. 5(a) and 5(d). It should be noted that only the defects on the visible side of the ellipsoid appear in these images, although full trajectories for all defects are represented in Fig. 5(g).

At the poles, the defects follow quasi-isolatitude trajectories, see Fig. 5(g) (left), while they maximize their separation distance due to elastic repulsion. These defects turn about the ellipsoid major axis assembling corotating swirls of the same handedness at the two poles of the ellipsoid; see Movie 1 in Supplemental Material [53]. The chirality of this motion is determined by spontaneous symmetry breaking and is randomly established when the AN is formed, remaining conserved over time.

To conciliate the defect dynamics at the poles, a counter-rotating defect belt appears simultaneously at the waist of the ellipsoid, setting a quadrupolar configuration of globally compensated torques. In the belt, oppositely charged defects form balanced pairs that do not contribute to the global topological charge of the system, which is $+2$, consistently with the global topological constraints for the ellipsoid [65,66]. The optical texture obtained by fluorescence imaging shows the formation of transversal bands (nearly perpendicular to major ellipsoidal axis) displaying mirror symmetry with respect to equatorial plane; see Figs. 5(a) and 5(d). This pattern is compatible with the smectic structure of the substrate, shown in Figs. 5(e) and 5(f), with the smectic layers setting the easy flow directions [15,16]; see Fig. 7.

Because extensile ANs are intrinsically unstable against bend deformations, such a transversally aligned state is susceptible to instabilities. This instability results in the appearance of four crimps perpendicular to the aligned field, with two visible in Fig. 5(b) as dark longitudinal lines, while the other two crimps are on the other side the droplet. This instability marks the onset of what we call the *translational regime*, where the two pairs of $+1/2$ defects concurrently migrate along the crimps from pole to pole, locally reorienting the director field along the major axis of the ellipsoid; see Figs. 5(b) and 5(g) (right) and Movie 1 in Supplemental Material [53]. As a result, the transversal bands get reoriented into longitudinal bands. The longitudinally aligned configuration is also unstable against bending, and the straight bands rapidly adopt parabolic shapes displaying mirror symmetry with respect to the

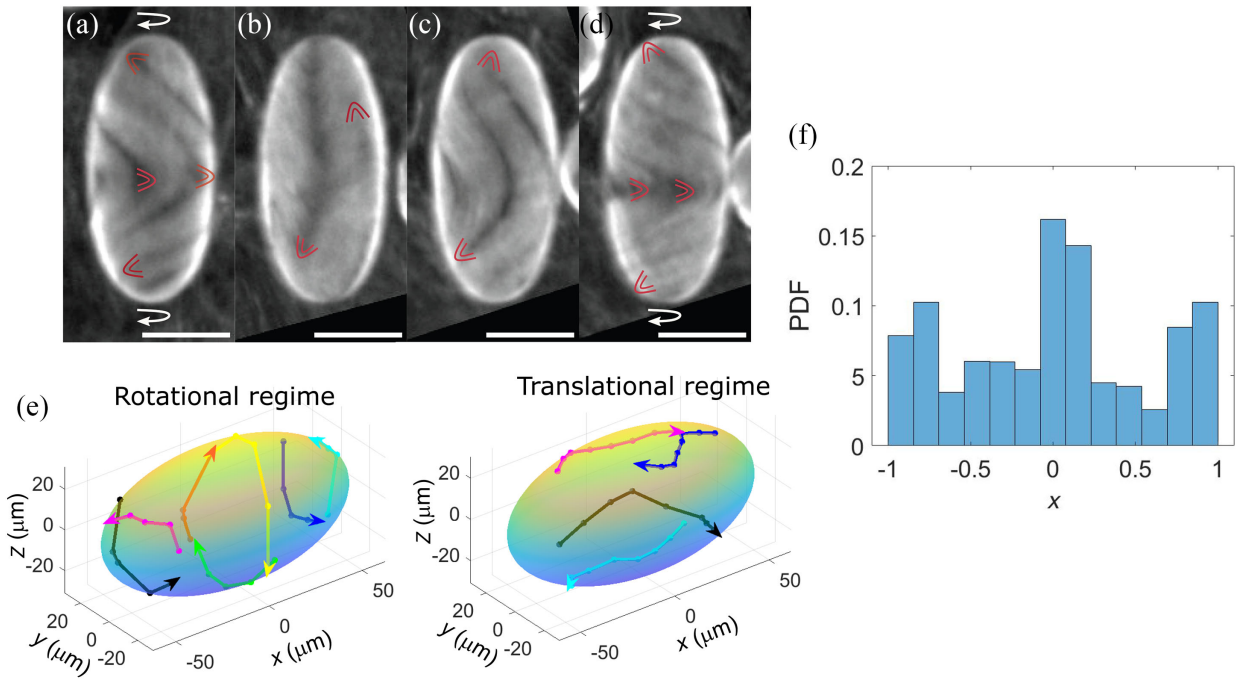

FIG. 5. Defect dynamics in the transient quadrupolar dynamic state. (a)–(d) Fluorescence confocal micrographs showing half-period of the system dynamics, from $t = 0$ (a) to $t = 23$ s (d). Red parabolic lines indicate $+1/2$ defects. Scale bars are 50 μm. (e) 3D reconstruction of the trajectory of $+1/2$ defects in the rotational and translational regimes in (a)–(d). (f) Normalized probability distribution histogram for the position of $+1/2$ defects along the major axis of the ellipsoid. The dynamics reported in (a)–(d) were observed for 50 droplets from independent experiments. The trend in (f) was observed for all the analyzed droplets (typically 10).

equatorial plane, a distinctive feature of the quadrupolar state; see Fig. 5(c). The equatorial belt with its accompanying population of positive and negative defects is progressively reconstituted, and the transversal bands reappear; see Fig. 5(d). This configuration is the same one shown in Fig. 5(b) with the pole defects having exchanged location. In the second half of the period, the whole process is repeated, and the two pairs of $+1/2$ defects regain their initial location. This incessant switching between rotationally and translationally moving phases persists for up to nearly two more hours, during which the active material continues to accumulate at the surface of the ellipsoid.

To investigate the effect of curvature on the defect dynamics, we analyzed the positioning of the defects in terms of their probability distribution along the major axis of the ellipsoid [Fig. 5(h)]. The histogram, which includes both positive and negative defects, aligns with two observations: Firstly, positive defects tend to cluster around regions of maximal curvature at the poles, and secondly, pairs of positive and negative defects with zero net topological charge persist in circulating along the equator. As mentioned above, this quadrupolar configuration is a transient state that eventually gives way to a more robust flow organization with bipolar symmetry. The transition to the bipolar state occurs when the equatorial defect band no longer reappears, inducing the counterrotation of the defects at the poles.

APPENDIX B: OSCILLATORY DYNAMICS OF TOPOLOGICAL DEFECTS IN THE FINAL DIPOLAR STATE

To visualize the oscillatory dynamics of the AN flows in the final dipolar dynamical state, we have reconstructed the 3D trajectory of the topological defects at the surface of an ellipsoid [see Fig. 1(f)), Movie 3, and the left-hand panel in Movie 4 in Supplemental Material [53]]. The representations were obtained by tracking simultaneously the defects on the top and bottom planes of the droplet (left-hand panel of Movie 3 in Supplemental Material), and projecting the resulting 2D trajectories on each of the two hemiellipsoidal surfaces, via a custom MATLAB program. As shown in Movies 3 and 4, oscillations appear as periodic cycles of defect rotation at the poles and translation from pole to pole. The defect configuration of each regime is well characterized by the distribution of θ_{ij}, which refers to the central angular distance between defect pairs (Fig. 6). During the translational regime [Figs. 6(a)–6(c)], the distribution is homogeneous, with θ_{ij} comprised between 50° and 170° and a maximal occurrence near 110°. In the rotational regime [Figs. 6(d)–6(f)], on the other hand,

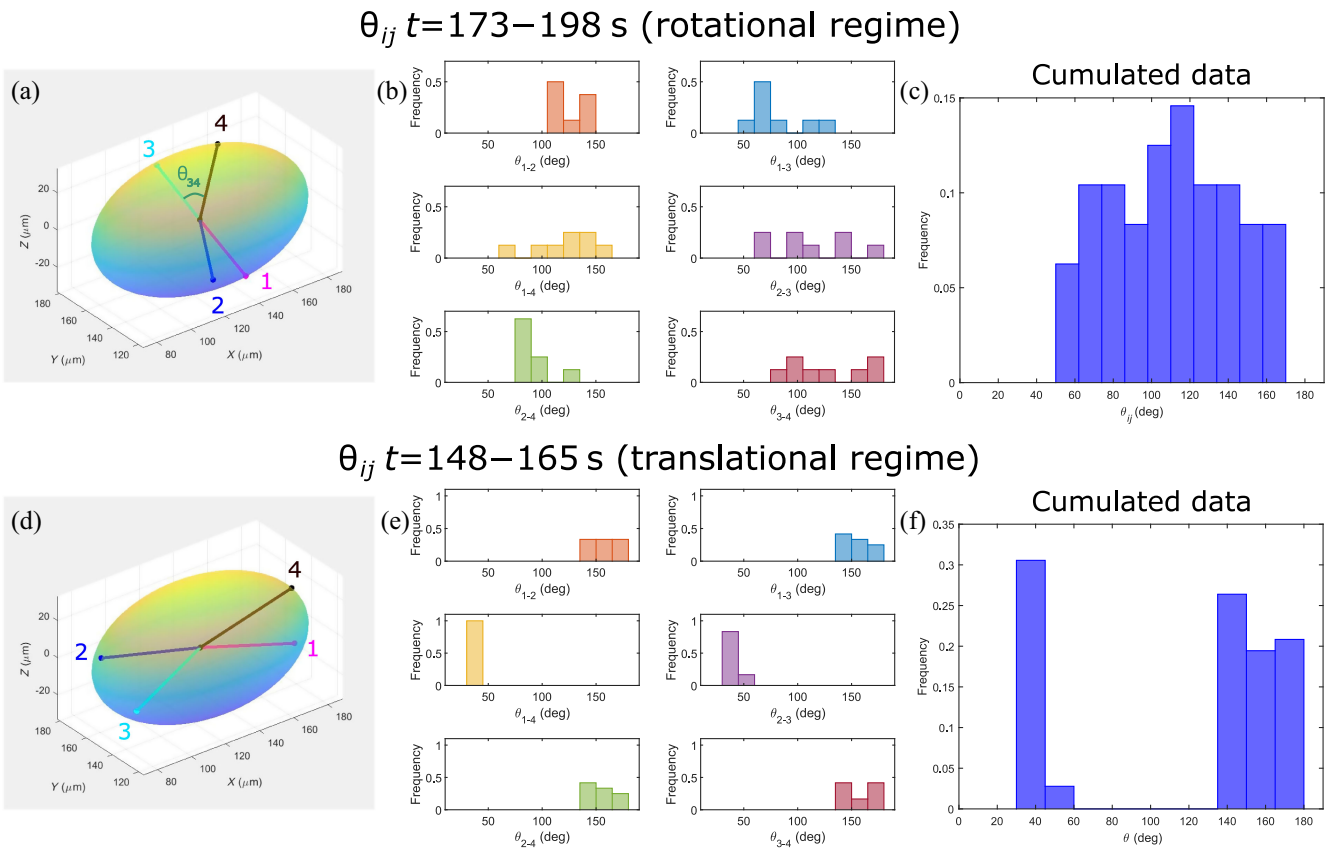

FIG. 6. Distributions of the relative central angles between pairs of defects θ_{ij} during (a)–(c) the translational regime and (d)–(f) the rotational regime.

defect pairs near the poles are separated by the angles θ_{14} and θ_{23}, with values below 60°, while opposite pairs of defects form angles θ_{12}, θ_{13}, θ_{24}, and θ_{34}, above 140°.

APPENDIX C: SIMULATION OF ACTIVE NEMATICS ON A 2D PLANAR INTERFACE WITH FRICTIONAL FORCES

We use numerical simulations to investigate how *frictional forces* control the dynamics of active nematics confined to a 2D planar interface. Initially, the director field is aligned along the x axis, as shown in Fig. 7(a). Once the extensile active force is applied on the system, bending instabilities yield the formation of topological defects and chaotic flows. However, the presence of frictional forces leads to regular spatiotemporal patterns in the flow and director fields, as shown in the remaining panels of Fig. 7.

We first examined the effect of incorporating an anisotropic frictional pattern where only the δ_{xx} component of the tensorial damping term in Eq. (5) is nonzero. This setup penalizes the flows parallel to the initial orientation of the director field (x axis) and provides an easy flow direction along the y axis. Initially, the system shows bending instabilities similar to those in the previous case [Fig. 7(b)]. However, due to the large elastic distortions and high shear stresses generated as a result of the formation of these elastic bands, at later times, the director undergoes additional distortions. The system finds it more energetically favorable to unbind pairs of $\pm 1/2$ defects and to form a stable nematic pattern with dominant splay deformation. The frictional forces imposed along the x axis impede the growth of additional bending instabilities and the nematic structure remains stable, as shown in Fig. 7(c). This result is closely related to the experimental observation made by Guillamat *et al.* in a microtubule-kinesin active nematic in contact with 8CB liquid crystal aligned via a magnetic field, where the high friction anisotropy imposed by the smectic layer led to the formation of antiparallel flowing lanes [14].

We then consider a case where the substrate in contact with the active layer does not impose a directional frictional anisotropy but a gradient in the friction magnitude. Here, the strength of the frictional damping force f_0 grows linearly along the x axis. This scenario can be achieved by having the active layer in contact with a substrate of varying viscosity. Figures 7(d) and 7(e) show that lanes of antiparallel flow develop with bands of different width. At the higher value of friction strength [higher values of x in Figs. 7(d) and 7(e)], the suppression of momentum

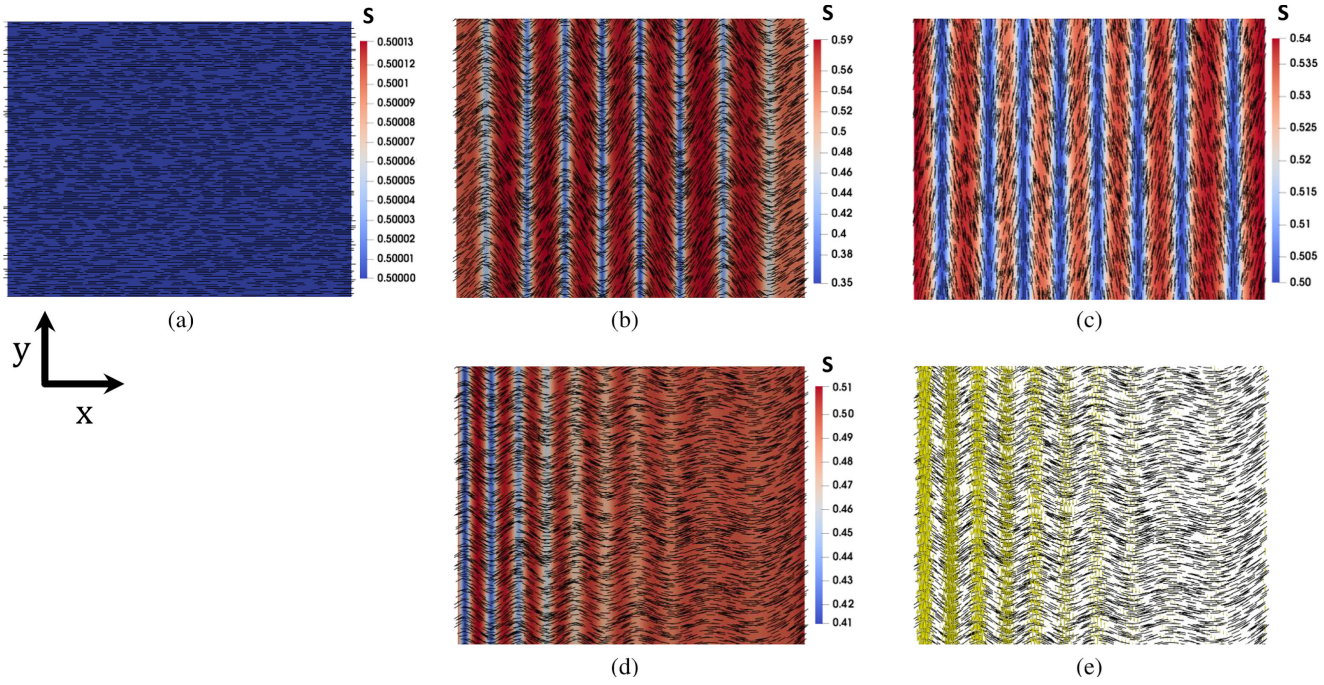

FIG. 7. The effect of friction on the director field and velocity profile of an active nematic layer confined on a 2D planar interface. Simulations were performed on a 200×200 two-dimensional lattice. The medium viscosity was set to $\eta = 1/6$, and the collective rotational viscosity to $\Gamma = 0.3$. The following parameters also were chosen: $A_0 = 0.05$, $L = 0.05$, $U = 3.0$ (giving $S = 0.5$). (a) The system was initialized with the director field oriented along the x axis and this was the starting point for all simulations. (b),(c) Nonuniform frictional forces are applied with the only nonzero coefficient of damping matrix being δ_{xx} ($f_0 = 0.3$ and $\zeta = 0.005$). (d),(e) A gradient of friction is applied, which grows linearly along the x axis [$\mathbf{f} = f_0\mathbf{I}$, $f_0 = 0.2(1 + x/L_x)$, and $\zeta = 0.012$]. A Poiseuille-like flow along the stripes is presented in (e) with $|v_{\max}| \approx 2.95 \times 10^{-3}$ in simulation units at the low friction region. Yellow arrows represent the local velocity field, with the magnitude of the velocity being normalized with its maximum value along the lines of high elastic distortions.

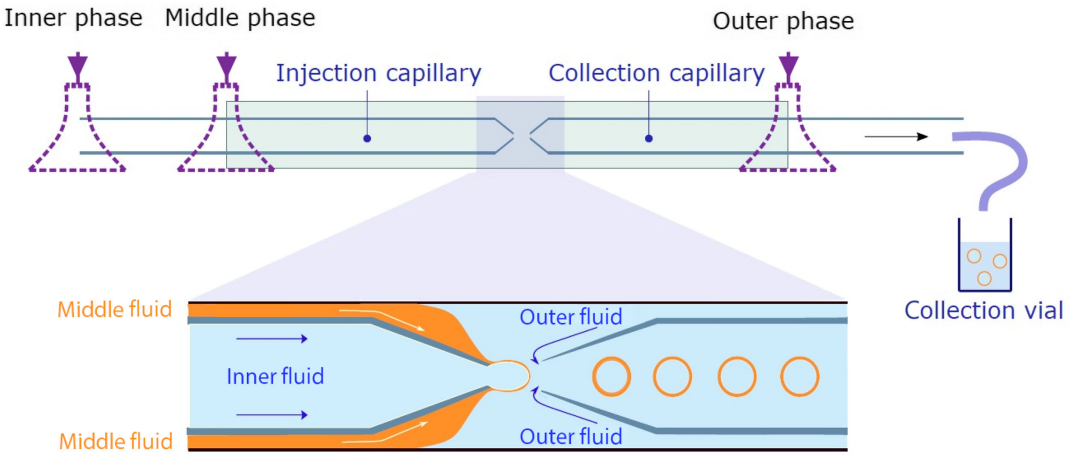

FIG. 8. Microfluidic fabrication of double emulsions. Schematic diagram of the axisymmetric microfluidic device used to generate double emulsions. This device consists of two tapered cylindrical glass capillaries inserted facing each other inside a square capillary. Dispensing needles are fixed at the three inlets of the device using epoxy glue. The inner, middle, and outer solutions are injected into each inlet using independent syringe pumps. A magnified view of the center of the device shows the formation of double emulsions in the dripping regime: The inner and middle fluids form a coaxial jet that is flow focused into the collection capillary by the outer phase. As the coaxial jet gets into the collection capillary it gets unstable and breaks up, producing monodisperse double emulsions.

propagation results in bands with a larger width along with smaller values of velocity.

With these examples we have demonstrated that by controlling the friction at a substrate, the otherwise chaotic active nematic flows can be tamed to precisely sculpt well-ordered spatiotemporal states and flow fields.

APPENDIX D: LIST OF SUPPLEMENTAL MOVIES

Movie 1: Dynamics of the active nematic in the quadrupolar transitory state. In the rotational regime, two pairs of $+1/2$ defects corotate at the poles, while pairs of oppositely charged defects circulate around the waist of the ellipsoid. This latitudinally aligned state is unstable against bending, leading to a translational regime in which positive defects migrate longitudinally from one pole to the other. Fluorescence images were acquired every 500 ms with a $\times 10$ objective using a confocal microscope.

Movie 2: Dynamics of the active nematic in the dipolar final state. In the rotational regime, two pairs of $+1/2$ defects counterrotate at the poles of the ellipsoid until a bend instability triggers their migration toward the opposite pole, setting the onset of the translational regime. Fluorescence images were acquired every 500 ms with a $\times 10$ objective using a confocal microscope.

Movie 3: Defect trajectories in the final dipolar state. Left: defect positions on the top and bottom surfaces of the ellipsoid. The movies were acquired using a fluorescence confocal microscope at a rate of 0.7 frame/s. Right: 3D reconstruction of the trajectory of the topological defects. This representation has been obtained by tracking the defects on the top and bottom planes of the droplet and projecting the resulting 2D trajectories on two hemiellipsoidal surfaces via a custom MATLAB program.

Movie 4: Oscillatory dynamics of the topological defects in the final dipolar dynamic state. Left: 3D reconstruction of the defect positions on the ellipsoidal surface and their evolution with time. The relative central angular distance between $+1/2$ defects results in six independent angles θ_{ij}, for the six different defect pairs i, j. Top right-hand panel: evolution of angular separations θ_{ij} between the six defect pairs. Each angle is assigned one color: θ_{12} orange, θ_{13} blue, θ_{14} yellow, θ_{23} purple, θ_{24} green, θ_{34} red. Bottom right-hand panel: oscillations of the average angle $\langle\theta\rangle$.

Movie 5: Simulated active nematic shell at a low activity and frictionless conditions. Two pairs of $1/2$ defects rotate on the antipodal points of a circumference at the poles of the ellipsoid while maximizing their separation distance.

Movie 6: Simulated active nematic shell at high activity and frictionless conditions. Under high activity, defects leave the poles and migrate toward the opposite pole. The handedness of the spirals at the poles is not preserved every half-period.

Movie 7: Simulated active nematic shell subject to a uniform frictional pattern. Defects counterrotate at the poles and then switch from one pole to the other while spiraling along the body of the ellipsoid. The handedness of spirals at the poles is inverted every half-period.

Movie 8: Rigid body rotation of the ellipsoidal shells in the dipolar state. Near a substrate, the counterrotating flows generated by the defects at the poles induce a rigid body rotation of the ellipsoid perpendicular to its main axis.

Movie 9: Trajectory of defects in an active nematic shell subject to a nonuniform frictional pattern. Defects counterrotate at the poles and then travel diagonally from one pole to the other. The handedness of spirals at the poles is preserved over time.

Movie 10: Simulated active nematic shell subject to a nonuniform frictional pattern. Defects counterrotate at the poles and then travel diagonally from one pole to the other. The handedness of spirals at the poles is preserved over time. The director field orients parallel to the equatorial plane during the rotational regime and realigns along the main axis during the translational regime.

[1] M. C. Marchetti, J. F. Joanny, S. Ramaswamy, T. B. Liverpool, J. Prost, M. Rao, and R. Aditi Simha, *Hydrodynamics of soft active matter*, Rev. Mod. Phys. **85**, 1143 (2013).

[2] D. Needleman and Z. Dogic, *Active matter at the interface between materials science and cell biology*, Nat. Rev. Mater. **2**, 17048 (2017).

[3] A. Doostmohammadi, J. Ignés-Mullol, J. M. Yeomans, and F. Sagués, *Active nematics*, Nat. Commun. **9**, 3246 (2018).

[4] R. Zhang, A. Mozaffari, and J. J. de Pablo, *Autonomous materials systems from active liquid crystals*, Nat. Rev. Mater. **6**, 437 (2021).

[5] Y. Maroudas-Sacks, E. Cohen, S. Hohmann, M. Politi, Y. Ideses, T. B. Saw, Y. Zlotnikov-Klionsky, M. Ehrlich, T. Vignaud, N. S. Gov *et al.*, *Topological defects in the nematic order of actin fibres as organization centres of hydra morphogenesis*, Nat. Phys. **17**, 251 (2021).

[6] O. J. Meacock, A. Doostmohammadi, K. R. Foster, J. M. Yeomans, and W. M. Durham, *Bacteria solve the problem of crowding by moving slowly*, Nat. Phys. **17**, 205 (2021).

[7] K. Copenhagen, R. Alert, N. S. Wingreen, and J. W. Shaevitz, *Topological defects promote layer formation in Myxococcus xanthus colonies*, Nat. Phys. **17**, 211 (2021).

[8] M.-A. Fardin and B. Ladoux, *Living proof of effective defects*, Nat. Phys. **17**, 172 (2021).

[9] S. P. Thampi, R. Golestanian, and J. M. Yeomans, *Active nematic materials with substrate friction*, Phys. Rev. E **90**, 062307 (2014).

[10] A. Doostmohammadi, M. F. Adamer, S. P. Thampi, and J. M. Yeomans, *Stabilization of active matter by flow-vortex lattices and defect ordering*, Nat. Commun. **7**, 10557 (2016).

[11] K. Thijssen, D. B. Hess, C. He, Z. Dogic, and M. L. Gardel, *Submersed micropatterned structures control active nematic flow, topology, and concentration*, Proc. Natl. Acad. Sci. U.S.A. **118**, e2106038118 (2021).

[12] A. Mozaffari, R. Zhang, N. Atzin, and J. J. de Pablo, *Defect spirograph: Dynamical behavior of defects in spatially patterned active nematics*, Phys. Rev. Lett. **126**, 227801 (2021).

[13] B. Martínez-Prat, R. Alert, F. Meng, J. Ignés-Mullol, J.-F. Joanny, J. Casademunt, R. Golestanian, and F. Sagués, *Scaling regimes of active turbulence with external dissipation*, Phys. Rev. X **11**, 031065 (2021).

[14] P. Guillamat, J. Ignés-Mullol, and F. Sagués, *Control of active liquid crystals with a magnetic field*, Proc. Natl. Acad. Sci. U.S.A. **113**, 5498 (2016).

[15] P. Guillamat, J. Ignés-Mullol, and F. Sagués, *Taming active turbulence with patterned soft interfaces*, Nat. Commun. **8**, 564 (2017).

[16] K. Thijssen, J. Yeomans, and A. Doostmohammadi, *Active nematics with anisotropic friction: The decisive role of the flow aligning parameter*, Soft Matter **16**, 2065 (2020).

[17] R. Zhang *et al.*, *Spatiotemporal control of liquid crystal structure and dynamics through activity patterning*, Nat. Mater. **20**, 875 (2021).

[18] X. Tang and J. V. Selinger, *Alignment of a topological defect by an activity gradient*, Phys. Rev. E **103**, 022703 (2021).

[19] R. Zhang, A. Mozaffari, and J. J. de Pablo, *Logic operations with active topological defects*, Sci. Adv. **8**, eabg9060 (2022).

[20] H. Wioland, F. G. Woodhouse, J. Dunkel, J. O. Kessler, and R. E. Goldstein, *Confinement stabilizes a bacterial suspension into a spiral vortex*, Phys. Rev. Lett. **110**, 268102 (2013).

[21] M. Ravnik and J. M. Yeomans, *Confined active nematic flow in cylindrical capillaries*, Phys. Rev. Lett. **110**, 026001 (2013).

[22] F. C. Keber, E. Loiseau, T. Sanchez, S. J. DeCamp, L. Giomi, M. J. Bowick, M. C. Marchetti, and Z. Dogic, *Topology and dynamics of active nematic vesicles*, Science **345**, 1135 (2014).

[23] R. Zhang, Y. Zhou, M. Rahimi, and J. J. de Pablo, *Dynamic structure of active nematic shells*, Nat. Commun. **7**, 13483 (2016).

[24] D. Khoromskaia and G. P. Alexander, *Vortex formation and dynamics of defects in active nematic shells*, New J. Phys. **19**, 103043 (2017).

[25] K.-T. Wu, J. B. Hishamunda, K. Mischaikow, S. Fraden, and M. J. Shelley, *Transition from turbulent to coherent flows in confined three-dimensional active fluids*, Science **355**, eaal1979 (2017).

[26] P. W. Ellis, D. J. G. Pearce, Y.-W. Chang, G. Goldsztein, L. Giomi, and A. Fernandez-Nieves, *Curvature-induced defect unbinding and dynamics in active nematic toroids*, Nat. Phys. **14**, 85 (2017).

[27] P. Guillamat, J. Ignes-Mullol, and F. Sagues, *Active nematic emulsions*, Sci. Adv. **4**, eaao1470 (2018).

[28] A. Sokolov, A. Mozaffari, R. Zhang, J. J. de Pablo, and A. Snezhko, *Emergence of radial tree of bend stripes in active nematics*, Phys. Rev. X **9**, 031014 (2019).

[29] D. J. G. Pearce, P. W. Ellis, A. Fernandez-Nieves, and L. Giomi, *Geometrical control of active turbulence in curved topographies*, Phys. Rev. Lett. **122**, 168002 (2019).

[30] A. Opathalage, M. M. Norton, S. Jung, J. V. Selinger, J. J. de Pablo, and R. N. Zia, *Self-organized dynamics and the transition to turbulence of confined active nematics*, Proc. Natl. Acad. Sci. U.S.A. **116**, 4788 (2019).

[31] J. Hardoüin, J. Laurent, T. Lopez-Leon, J. Ignés-Mullol, and F. Sagués, *Active microfluidic transport in two-dimensional handlebodies*, Soft Matter **16**, 9230 (2020).

[32] M. Rajabi, H. Baza, T. Turiv, and O. Lavrentovich, *Directional self-locomotion of active droplets enabled by nematic environment*, Nat. Phys. **17**, 260 (2021).

[33] T. Lubensky and J. Prost, *Orientational order and vesicle shape*, J. Phys. II (France) **2**, 371 (1992).

[34] T. Lopez-Leon, V. Koning, K. Devaiah, V. Vitelli, and A. Fernandez-Nieves, *Frustrated nematic order in spherical geometries*, Nat. Phys. **7**, 391 (2011).

[35] Y. H. Zhang, M. Deserno, and Z. C. Tu, *Dynamics of active nematic defects on the surface of a sphere*, Phys. Rev. E **102**, 012607 (2020).

[36] A. T. Brown, *A theoretical phase diagram for an active nematic on a spherical surface*, Soft Matter **16**, 4682 (2020).

[37] S. Henkes, M. C. Marchetti, and R. Sknepnek, *Dynamical patterns in nematic active matter on a sphere*, Phys. Rev. E **97**, 042605 (2018).

[38] F. Alaimo, C. Köhler, and A. Voigt, *Curvature controlled defect dynamics in topological active nematics*, Sci. Rep. **7**, 5211 (2017).

[39] S. Ehrig, J. Ferracci, R. Weinkamer, and J. W. C. Dunlop, *Curvature-controlled defect dynamics in active systems*, Phys. Rev. E **95**, 062609 (2017).

[40] M. J. Bowick and L. Giomi, *Two-dimensional matter: Order, curvature and defects*, Adv. Phys. **58**, 449 (2009).

[41] M. A. Bates, G. Skačej, and C. Zannoni, *Defects and ordering in nematic coatings on uniaxial and biaxial colloids*, Soft Matter **6**, 655 (2010).

[42] S. Kralj, R. Rosso, and E. G. Virga, *Curvature control of valence on nematic shells*, Soft Matter **7**, 670 (2011).

[43] E. J. L. de Oliveira, I. N. de Oliveira, M. L. Lyra, and L. V. Mirantsev, *Tunable topological valence in nematic shells on spherocylindrical colloidal particles*, Phys. Rev. E **93**, 012703 (2016).

[44] D. Jesenek, S. Kralj, R. Rosso, and E. G. Virga, *Defect unbinding on a toroidal nematic shell*, Soft Matter **11**, 2434 (2015).

[45] E. J. Hemingway, P. Mishra, M. C. Marchetti, and S. M. Fielding, *Correlation lengths in hydrodynamic models of active nematics*, Soft Matter **12**, 7943 (2016).

[46] A. Utada, E. Lorenceau, D. R. Link, P. D. Kaplan, H. A. Stone, and D. A. Weitz, *Monodisperse double emulsions generated from a microcapillary device*, Science **308**, 537 (2005).

[47] T. Lopez-Leon, A. Fernandez-Nieves, M. Nobili, and C. Blanc, *Nematic-smectic transition in spherical shells*, Phys. Rev. Lett. **106**, 247802 (2011).

[48] T. Sanchez, D. T. N. Chen, S. J. DeCamp, M. Heymann, and Z. Dogic, *Spontaneous motion in hierarchically assembled active matter*, Nature (London) **491**, 431 (2012).

[49] S. J. DeCamp, G. S. Redner, A. Baskaran, M. F. Hagan, and Z. Dogic, *Orientational order of motile defects in active nematics*, Nat. Mater. **14**, 1110 (2015).

[50] B. Martínez-Prat, J. Ignés-Mullol, J. Casademunt, and F. Sagués, *Selection mechanism at the onset of active turbulence*, Nat. Phys. **15**, 362 (2019).
[51] T. Kampmann, H. Boltz, and J. Kierfeld, *Controlling adsorption of semiflexible polymers on planar and curved substrates*, J. Chem. Phys. **139**, 034903 (2013).
[52] S. Stepanow, *Adsorption of a semiflexible polymer onto interfaces and surfaces*, J. Chem. Phys. **115**, 1565 (2001).
[53] See Supplemental Material at http://link.aps.org/supplemental/10.1103/PhysRevX.14.031049 for movies of experiments and simulations.
[54] R. L. B. Selinger, A. Konya, A. Travesset, and J. V. Selinger, *Monte Carlo studies of the* XY *model on two-dimensional curved surfaces*, J. Phys. Chem. B **115**, 13989 (2011).
[55] M. Kralj, M. Kralj, and S. Kralj, *Topological defects in nematic liquid crystals: Laboratory of fundamental physics*, Phys. Status Solidi A **218**, 2000752 (2021).
[56] R. D. Kamien, D. R. Nelson, C. D. Santangelo, and V. Vitelli, *Extrinsic curvature, geometric optics, and lamellar order on curved substrates*, Phys. Rev. E **80**, 051703 (2009).
[57] V. Vitelli and D. R. Nelson, *Defect generation and deconfinement on corrugated topographies*, Phys. Rev. E **70**, 051105 (2004).
[58] L. A. Hoffmann, L. N. Carenza, J. Eckert, and L. Giomi, *Theory of defect-mediated morphogenesis*, Sci. Adv. **8**, eabk2712 (2022).
[59] M. Prasad, N. Obana, S.-Z. Lin, S. Zhao, K. Sakai, C. Blanch-Mercader, J. Prost, N. Nomura, J.-F. Rupprecht, J. Fattaccioli, and A. S. Utada, *Alcanivorax borkumensis biofilms enhance oil degradation by interfacial tubulation*, Science **381**, 748 (2023).
[60] T. B. Saw, A. Doostmohammadi, V. Nier, L. Kocgozlu, S. Thampi, Y. Toyama, P. Marcq, C. T. Lim, J. M. Yeomans, and B. Ladoux, *Topological defects in epithelia govern cell death and extrusion*, Nature (London) **544**, 212 (2017).
[61] P. Guillamat, C. Blanch-Mercader, G. Pernollet, K. Kruse, and A. Roux, *Integer topological defects organize stresses driving tissue morphogenesis*, Nat. Mater. **21**, 588 (2022).
[62] A. W. C. Lau, A. Prasad, and Z. Dogic, *Condensation of isolated semi-flexible filaments driven by depletion interactions*, Europhys. Lett. **87**, 48006 (2009).
[63] D. Marenduzzo, E. Orlandini, and J. M. Yeomans, *Hydrodynamics and rheology of active liquid crystals: A numerical investigation*, Phys. Rev. Lett. **98**, 118102 (2007).
[64] R. Zhang, N. Kumar, J. L. Ross, M. L. Gardel, and J. J. de Pablo, *Interplay of structure, elasticity, and dynamics in actin-based nematic materials*, Proc. Natl. Acad. Sci. U.S.A. **115**, E124 (2018).
[65] H. Hopf, *Vektorfelder in n-dimensionalen-mannigfaltigkeiten*, Math. Ann. **96**, 225 (1927).
[66] H. Poincaré, *Mémoire sur les courbes définies par une équation différentielle (i)*, J. Math. Pures Appl. **7**, 375 (1881), http://www.numdam.org/item/JMPA_1881_3_7__375_0/.